PHYSICAL REVIEW B **71**, 195321 (2005)

Excitonic wave packet dynamics in semiconductor photonic-crystal structures

B. Pasenow, M. Reichelt, T. Stroucken, T. Meier, and S. W. Koch
Department of Physics and Material Sciences Center, Philipps University, Renthof 5, D-35032 Marburg, Germany

(Received 14 December 2004; revised manuscript received 1 March 2005; published 24 May 2005)

Significant aspects of the light–matter interaction can be strongly modified in suitably designed systems consisting of semiconductor nanostructures and dielectric photonic crystals. To analyze such effects, a microscopic theory is presented, which is capable of describing the optoelectronic properties of such hybrid systems via a self-consistent solution of the dynamics of the optical field and the photoexcitations of the material. The theory is applied to investigate the local excitonic resonances, which arise as a consequence of the modified Coulomb interaction in the vicinity of a structured dielectric medium. The excitation of a coherent superposition of the spatially inhomogeneous optical transitions induces an intricate wave packet dynamics. In the presence of dephasing and relaxation processes, the coherent oscillations are damped and the photoexcited carriers relax into spatially inhomogeneous quasi-equilibrium distributions.

DOI: 10.1103/PhysRevB.71.195321 PACS number(s): 71.35.Cc, 42.50.Md, 42.70.Qs, 71.35.−y

I. INTRODUCTION

Photonic crystals, i.e., periodically structured dielectric materials, can be used to tailor the eigenmodes of the transverse electromagnetic field.[1–5] Since the light–matter interaction in atoms, molecules, and solids is governed by this transverse part of the field, the optical material properties can be drastically changed with suitably designed photonic-crystal structures. Using a photonic band gap one can suppress the spontaneous emission and thus increase the radiative lifetime of optical excitations by several orders of magnitude.[1,2,6–8] By the interaction with localized defect modes in photonic crystals novel strong coupling effects can be achieved.[9–12]

In this context, semiconductor heterostructures are of particular interest not only because they can be grown with almost molecular precision but also because of their strong excitonic resonances.[13,14] The quantum efficiency of well-designed optoelectronic semiconductor devices approaches the fundamental radiative lifetime limit and combinations of semiconductor nanostructures and photonic crystals allow for the possibility to optimize characteristics of light-emitting diodes and lasers.[10,11,15–21] In addition to this application potential, however, semiconductor photonic-crystal structures are also of interest in the context of fundamental physics. For example, it has been demonstrated that the reduced spontaneous emission due to photonic crystals results in strong modifications of the exciton statistics and Coulomb many-particle correlations inside a semiconductor material.[22]

Beside the transverse field, also the longitudinal electromagnetic field, i.e., the Coulomb potential between charged particles, can be modified significantly in suitably designed semiconductor photonic-crystal structures.[23–26] In such hybrid systems, induced surface polarizations alter the optical semiconductor properties in comparison to a spatially homogeneous excitation configuration, resulting in dielectric shifts of the band gap and the energetic position of the exciton resonance.[27,28] Furthermore, spatially inhomogeneous quasi-equilibrium carrier populations can be obtained, which may substantially influence the quasi-equilibrium gain spectra of laser structures.[26] The periodic modulation of the optical properties may even result in superradiant emission.[29,30]

In this paper, we present and apply a microscopic approach, which is capable of describing the optical properties of spatially inhomogeneous semiconductor photonic-crystal structures. In most of our previous treatment,[24–26] where we have concentrated on longitudinal effects, the transverse optical field has been assumed to be homogeneous. In contrast, here, the coupled dynamics of the field and the material excitations are treated self-consistently by evaluating the coupled Maxwell semiconductor Bloch equations (MS-BEs) by numerical integration. In each time step, Maxwells' equations are solved using the finite-difference time-domain (FDTD) method[31] with complex fields. The semiconductor Bloch equations (SBE),[13] which are used here in a real-space basis in order to describe spatially inhomogeneous situations, are integrated using the standard leap-frog algorithm.[32] With this combination it is possible to use the rotating wave approximation for the semiconductor excitations and to restrict the analysis to resonant excitations. This approach has successfully been applied in Ref. 33 to analyze optical absorption spectra in the presence of quasi-equilibrium electron and hole populations. Here, it is extended and used to study besides the dynamics of the optical polarization also the spatiotemporal evolution of photoexcited populations.

In particular, we analyze the local absorption spectra and discuss optical excitation of a coherent superposition of spatially inhomogeneous excitonic resonances. After the incident laser pulse has decayed, the photoexcitations of the semiconductor material oscillate coherently and display an intricate wave packet dynamics. The predicted effects should be measurable by ultrafast nonlinear optical spectroscopy where they show up as temporal modulations of the signal.[34–36] In the course of time, the coherent oscillations are damped due to dephasing and relaxation processes. Therefore, in the long time limit the photoexcited carriers approach quasi-equilibrium distributions. Due to the modified Coulomb interaction, these carrier distributions are inhomogeneous in space.

In Sec. II of this paper the microscopic approach and the self-consistent analysis of the light–matter interaction in semiconductor photonic-crystal structures is described. Numerical results on the excitonic absorption in spatially inhomogeneous situations, the coherent dynamics of excitonic wave packets, and the decay of the coherent oscillations due to dephasing and relaxation processes are presented and discussed in Sec. III. The most important results are briefly summarized in Sec. IV.

II. SPATIALLY INHOMOGENEOUS MAXWELL-SEMICONDUCTOR BLOCH EQUATIONS

In this section, we present our theoretical approach, which provides a self-consistent description of the coupled dynamics of the electromagnetic field and the optical material excitations in semiconductor photonic-crystal structures. Within a semiclassical treatment, the material system is described quantum mechanically whereas the dynamics of the electromagnetic field is treated classically. As shown in Sec. II A, the transverse components of the field are determined by Maxwell's equations with a spatially varying dielectric function. These equations include the coupling to the optical material polarization whose time derivative appears as a source in the equation for the electric field. Besides the time-dependent field, also the static field, i.e., the Coulomb interaction among charged particles, is modified in the vicinity of a spatially structured dielectric environment. The generalized Coulomb potential describing the interaction of the charge carriers in a semiconductor near a photonic crystal can be obtained by solving an integral equation,[23–26] as described in Sec. II B. The Hamiltonian, which governs the dynamics of photoexcited electrons and holes in the semiconductor, is introduced in Sec. II C. The equations of motion describing the dynamics of the optical material excitations are presented in Sec. II D where also the inclusion of nonradiative dephasing and relaxation is discussed.

A. Inhomogeneous Maxwell's equations in photonic crystals

Propagation of electromagnetic waves through a macroscopic material is governed by the inhomogeneous Maxwell equations

$$\nabla \cdot \mathbf{D} = \rho, \tag{1}$$

$$\nabla \cdot \mathbf{B} = 0, \tag{2}$$

$$\nabla \times \mathbf{E} + \frac{\partial}{\partial t}\mathbf{B} = 0, \tag{3}$$

$$\nabla \times \mathbf{H} - \frac{\partial}{\partial t}\mathbf{D} = \mathbf{j}. \tag{4}$$

Here, $\mathbf{E}$ and $\mathbf{H}$ are the macroscopic electric and magnetic fields, $\mathbf{D}$ and $\mathbf{B}$ are the dielectric displacement and magnetic induction fields, and ρ and $\mathbf{j}$ are the free charges and currents in the material, respectively. Maxwell's equations constitute a set of 8 inhomogeneous differential equations for the 12 field components, where the charges and currents act as source terms. For an interacting system, Maxwell's equations are solved together with the equations of motion for the particle charges and currents, that are in turn driven by the optical fields $\mathbf{E}$ and $\mathbf{H}$. In order to solve these equations, we need the constitutive relations $\mathbf{D}=\mathbf{D}[\mathbf{E}]$ and $\mathbf{B}=\mathbf{D}[\mathbf{H}]$ relating the macroscopic to the microscopic fields. In general, the constititive relations can be arbitrarily complicated, relating the components of the dielectric displacement and magnetic induction in a nonlocal, anisotropic, frequency dependent, and nonlinear manner to the components of the electric and magnetic fields. As we are interested in optics in dielectric photonic crystals, we shall assume nonmagnetic media in the following, i.e., $\mathbf{B}=\mu_0\mathbf{H}$. For the dielectric displacement, we make the ansatz

$$\mathbf{D} = \epsilon_0 \epsilon(\mathbf{r})\mathbf{E}, \tag{5}$$

where the photonic crystal structure is described via a periodically varying dielectric function $\epsilon(\mathbf{r})$, which is assumed to be a local, scalar, and frequency independent. All other contributions are mediated by the resonant light–matter interaction and are determined by explicitly solving the microscopic equations of motion for the particle system.

As is well known, the current and charge density couple to the vector and scalar potential, respectively, rather than to the electromagnetic field components. These are introduced with the aid of the homogeneous Maxwell equations as $\mathbf{B} = \nabla \times \mathbf{A}$, $\mathbf{E} = -\dot{\mathbf{A}} - \nabla \phi$. Inserting the potentials in the inhomogeneous Maxwell equations, we obtain

$$\nabla \times \nabla \times \mathbf{A} + \frac{\epsilon(\mathbf{r})}{c^2}\frac{\partial^2}{\partial t^2}\mathbf{A} = -\frac{\epsilon(\mathbf{r})}{c^2}\nabla \dot{\phi} + \mu_0 \mathbf{j}, \tag{6}$$

$$\nabla \cdot \epsilon(\mathbf{r})\left(\frac{1}{c}\frac{\partial}{\partial t}\mathbf{A} + \nabla \phi\right) = -\rho/\epsilon_0. \tag{7}$$

From Eq. (7), it is obvious that the scalar potential is not truly an independent variable, but is determined by the vector potential, the dielectric function, and the charge density. In homogeneous media, the scalar potential can be expressed in terms of the charge density only with the aid of the Coulomb gauge $\nabla \cdot \mathbf{A}=0$. Within a semiclassical treatment, the interactions induced by this part of the electric field are treated fully quantum mechanically, whereas that part of the electromagnetic field that is associated with the vector potential is treated classically. In inhomogeneous media, the standard Coulomb gauge leads to a nonvanishing scalar potential even in the absence of external charges. Therefore, it is advantageous to introduce the generalized Coulomb gauge $\nabla \cdot \epsilon(\mathbf{r})\mathbf{A}=0$.[37,38] This gauge corresponds to a division into a transverse and longitudinal part of the dielectric displacement rather than the electric field, i.e., $\mathbf{D}=\mathbf{D}_T+\mathbf{D}_L$ with $\mathbf{D}_T = -\epsilon(\mathbf{r})\dot{\mathbf{A}}$ and $\mathbf{D}_L = -\epsilon(\mathbf{r})\nabla \phi$. Within a semiclassical description, the transverse part of the dielectric displacement and the magnetic field are treated classically and obey the coupled wave equations

$$\nabla \times \frac{\mathbf{D}_T}{\epsilon_0 \epsilon(\mathbf{r})} + \frac{\partial}{\partial t}\mathbf{B} = 0, \tag{8}$$

$$\nabla \times \mathbf{B} - \mu_0 \frac{\partial}{\partial t}\mathbf{D}_T = \mu_0 \mathbf{j}_T, \tag{9}$$

where $\mathbf{j}_T$ is the transverse part of the current, which appears as a source term for the classical part of the electromagnetic field.

In our numerical solutions, the spatiotemporal evolution of the electromagnetic field is obtained by solving the FDTD equations.[31] These equations are self-consistently integrated together with the SBE, see Sec. II D, that determine the material excitations.

B. The Coulomb interaction

Within our semiclassical treatment, the field energy associated with the longitudinal part of the dielectric displacement is treated quantum mechanically and results in the Coulomb interaction among charged particles. Inserting the definition of $\mathbf{D}_L$ and Eq. (1) into the expression for the field energy, we obtain

$$\begin{aligned} H_C &= \frac{1}{2}\int d^3r \frac{\mathbf{D}_L \cdot \mathbf{D}_L}{\epsilon_0 \epsilon(\mathbf{r})} \\ &= -\frac{1}{2}\int d^3r\, \nabla\phi \cdot \mathbf{D}_L \\ &= \frac{1}{2}\int d^3r\, \phi\, \nabla \cdot \mathbf{D}_L \\ &= \frac{1}{2}\int d^3r\, \phi(\mathbf{r})\rho(\mathbf{r}). \end{aligned} \tag{10}$$

The scalar potential is the solution of a generalized Poisson equation

$$-\nabla \cdot [\epsilon(\mathbf{r})\nabla\phi(\mathbf{r},t)] = \rho(\mathbf{r},t)/\epsilon_0, \tag{11}$$

with the charge density $\rho(\mathbf{r},t)$ as inhomogeneity. Defining the generalized Coulomb potential $V^C(\mathbf{r},\mathbf{r}')$ as the solution of the generalized Poisson equation with a δ-function inhomogeneity

$$-\nabla \cdot [\epsilon(\mathbf{r})\nabla V^C(\mathbf{r},\mathbf{r}')] = \delta(\mathbf{r}-\mathbf{r}')/\epsilon_0, \tag{12}$$

the scalar potential can be expressed as

$$\phi(\mathbf{r},t) = \int d^3r'\, V^C(\mathbf{r},\mathbf{r}')\rho(\mathbf{r}',t), \tag{13}$$

yielding

$$H_C = \frac{1}{2}\int d^3r \int d^3r'\, \rho(\mathbf{r})V^C(\mathbf{r},\mathbf{r}')\rho(\mathbf{r}') \tag{14}$$

for the Coulomb energy. The generalized Coulomb potential describes the interaction among charged particles in an inhomogeneous dielectric environment.

With the exception of a few analytically solvable geometries, like, e.g., two dielectric half spaces separated by a plane or a single sphere embedded into a material of different dielectric constant,[39] Eq. (12) has to be solved numerically for general situations. For this purpose, it is advantageous to start from the integral equation[23,26]

$$V^C(\mathbf{r},\mathbf{r}') = -\frac{1}{4\pi}\int d^3r''\, \nabla'' \frac{1}{|\mathbf{r}''-\mathbf{r}|} \cdot \mathbf{E}_l(\mathbf{r}'',\mathbf{r}'), \tag{15}$$

where $\mathbf{E}_l(\mathbf{r},\mathbf{r}') = -\nabla V^C(\mathbf{r},\mathbf{r}')$ is the electric field at the position $\mathbf{r}$ due to a unit charge at $\mathbf{r}'$. If the dielectric function is piecewise constant, which is usually the case in photonic crystals, one can partially evaluate the volume integral appearing in Eq. (15) and use the boundary conditions for the electric field $\mathbf{E}_l$ and the dielectric displacement $\mathbf{D}_l$ at the interfaces ∂D_{ij}, which separate regions D_i and D_j of different dielectric functions. As shown in Ref. 23, one obtains

$$\begin{aligned} V^C(\mathbf{r},\mathbf{r}') &= \frac{1}{4\pi\epsilon_0}\frac{1}{\epsilon(\mathbf{r}')}\frac{1}{|\mathbf{r}-\mathbf{r}'|} \\ &\quad - \frac{1}{4\pi\epsilon_0}\sum_{ij}\left(\frac{1}{\epsilon_i}-\frac{1}{\epsilon_j}\right)\int_{\partial D_{ij}} da''\frac{1}{|\mathbf{r}''-\mathbf{r}|}\mathbf{n}_i'' \cdot \mathbf{D}_l(\mathbf{r}'',\mathbf{r}') \\ &= V_0(\mathbf{r},\mathbf{r}') + \delta V(\mathbf{r},\mathbf{r}'), \end{aligned} \tag{16}$$

where $\mathbf{n}_i''$ denotes the unit vector normal to the surface at $\mathbf{r}''$. According to Eq. (16), V^C is given by the sum of two contributions. V_0 has the usual $1/|\mathbf{r}-\mathbf{r}'|$ spatial variation and is additionally statically screened with the local value of the dielectric function $1/\epsilon(\mathbf{r}')$. The second term, δV, appears as a result of induced surface polarizations at the interfaces ∂D_{ij}, which separate the regions of different ϵ, over which is integrated. The magnitude of δV may be large, if the dielectric contrast is large and, in particular, if the charge is close to an interface since in this case the interaction with the induced surface polarizations is strong.

In contrast to the situation in spatially homogeneous media, the generalized Coulomb potential is a function not only of the relative coordinate $\mathbf{r}_{\mathrm{rel}} = \mathbf{r}-\mathbf{r}'$ but also of the center of mass coordinate $\mathbf{r}_{\mathrm{c.m.}} = (m_1/M)\mathbf{r} + (m_2/M)\mathbf{r}'$ with $m_1 + m_2 = M$. The dependence of the generalized Coulomb potential on $\mathbf{r}_{\mathrm{c.m.}}$ obeys the same symmetry properties as the dielectric function $\epsilon(\mathbf{r})$. In systems where the dielectric function is varying periodically in space, e.g., in photonic crystals, also V^C exhibits this periodicity.

The generalized Coulomb potential can be evaluated numerically using an integral equation for the dielectric displacement $\mathbf{D}_l$ at the interfaces ∂D_{ij}. This equation can be obtained by applying $\mathbf{n}_i(\mathbf{r}) \cdot \nabla$ to Eq. (16), where $\mathbf{n}_i(\mathbf{r})$ denotes the unit vector normal to the surface at $\mathbf{r}$. Defining the normal component of the dielectric displacement by

$$D_n(\mathbf{r},\mathbf{r}') = \mathbf{n}_i(\mathbf{r}) \cdot \mathbf{D}_l(\mathbf{r},\mathbf{r}'), \tag{17}$$

one obtains[25,26]

$$\begin{aligned} D_n(\mathbf{r},\mathbf{r}') &= \mathbf{n}_i(\mathbf{r}) \cdot \frac{\mathbf{r}-\mathbf{r}'}{|\mathbf{r}-\mathbf{r}'|^3} + \lim_{\gamma \to 0_+}\frac{1}{4\pi}\left(1-\frac{\epsilon_1}{\epsilon_2}\right) \\ &\quad \times \int_{\partial D_{ij}} da''\, \mathbf{n}_i(\mathbf{r}) \cdot \frac{\mathbf{r}_\gamma - \mathbf{r}''}{|\mathbf{r}_\gamma - \mathbf{r}''|} D_n(\mathbf{r}'',\mathbf{r}'), \end{aligned} \tag{18}$$

with $\mathbf{r}_\gamma = \mathbf{r} - \gamma\mathbf{n}_i(\mathbf{r})$. To determine D_n, Eq. (18) can be solved by matrix inversion on a grid in real-space using the Nystrom method.[32] Inserting this solution into Eq. (16) allows one to determine the generalized Coulomb potential V^C in all spatial regions of interest.

C. Hamilton operator

The Hamiltonian describing the optical properties of semiconductors and semiconductor nanostructures consists of three terms[13]

$$\hat{H} = \hat{H}_0 + \hat{H}_I + \hat{H}_C. \tag{19}$$

Here, $\hat{H}_0$ contains the single-particle band structure, $\hat{H}_I$ denotes the interaction of the semiconductor with the classical part of the electromagnetic field, and $\hat{H}_C$ describes the many-body Coulomb interaction among charged particles including the modifications due to the dielectric structuring discussed earlier. According to the minimal coupling approach, we have

$$\hat{H}_0 + \hat{H}_I = \int d^3r\,\psi^\dagger(\mathbf{r})\left[\frac{1}{2m_0}(\mathbf{p} - e\mathbf{A})^2 + V_G(\mathbf{r}) + V_{\text{conf}}(\mathbf{r})\right]\psi(\mathbf{r}). \tag{20}$$

Here, m_0 is the electron mass, V_G is the periodic lattice potential, V_{conf} is the confinement potential in a system of reduced dimensionality, and $\psi^\dagger$, ψ are the Heisenberg creation and annihilation operators for the electrons. The total particle current $\mathbf{j}$ entering as source term into the dynamical equations for the transverse field components is obtained from the interaction Hamiltonian via

$$\mathbf{j} = -\frac{1}{\mu_0}\frac{\delta\hat{H}_I}{\delta\mathbf{A}} = -\frac{e}{\mu_0 m_0}\psi^\dagger\left(\mathbf{p} - \frac{e}{c}\mathbf{A}\right)\psi. \tag{21}$$

Using the Heisenberg equation of motion for the field operators, it is easily verified that the current can be expresses alternatively as the time derivative of the polarization, i.e.,

$$\mathbf{j} = \frac{1}{\mu_0}\frac{\partial}{\partial t}\mathbf{P} = \frac{1}{\mu_0}\frac{\partial}{\partial t}\psi^\dagger e\mathbf{r}\psi = -\frac{1}{\mu_0}\frac{\delta}{\delta\mathbf{A}}\int d^3r\,\dot{\mathbf{P}}\mathbf{A}. \tag{22}$$

Since the total Hamiltonian can be changed by a total time derivative without altering the equations of motion, the dynamics of the system can also be obtained from the dipole interaction Hamiltonian

$$H_I = -\int d^3r\,\mathbf{E}_T\cdot\mathbf{P}, \tag{23}$$

where we used the notation $\mathbf{E}_T = -\dot{\mathbf{A}} = \mathbf{D}_T/\epsilon_0\epsilon(\mathbf{r})$. Note that $\mathbf{E}_T$ is not transverse but corresponds to the classical part of the electromagnetic field. This is not yet the dipole approximation but is exact. The macroscopic polarization current $(\partial/\partial t)\langle\mathbf{P}\rangle$ has to be computed from the Heisenberg equations of motion

$$i\hbar\frac{\partial}{\partial t}\langle\mathbf{P}\rangle = \langle[\mathbf{P}, H]\rangle. \tag{24}$$

In order to solve these equations, it is convenient to expand the creation and annihilation operators in terms of eigenfunctions of H_0. In general, the eigenfunctions of H_0 in a crystal can be written as products of lattice periodic functions $u_{\mu,\mathbf{k}}(\mathbf{r})$ and the envelope funtions $\phi_{\mu,\mathbf{k}}(\mathbf{r}) = \exp(i\mathbf{k}_\parallel\cdot\mathbf{r}_\parallel)\varphi_{\mu,\mathbf{k}_\perp}(\mathbf{r}_\perp)$ that vary on a length scale much larger than the lattice constant, i.e., $\psi(\mathbf{r}) = \Sigma_{\mu,\mathbf{k}} u_{\mu,\mathbf{k}}(\mathbf{r})\phi_{\mu,\mathbf{k}}(\mathbf{r})a_{\mu,\mathbf{k}}$. Here, μ denotes the band index, $\mathbf{k}$ all other relevant quantum numbers, $\mathbf{r}_\parallel$ are the coordinates in the extended directions of the semiconductor nanostructure, $\mathbf{r}_\perp$ the coordinates perpendicular to the structure, and $\varphi_{\mu,\mathbf{k}}$ is the confinement function. For simplicity, we restrict the analysis to a two-band situation considering only the lowest confinement subbands, i.e., a single conduction and a single valence band, respectively. It is, however, straightforward to extend this approach to multiple bands by including summations over the relevant bands in the following expressions. Applying the electron hole picture by $c_\mathbf{k} = a_{c,\mathbf{k}}$ and $d_\mathbf{k} = a^+_{v,-\mathbf{k}}$, the single particle part of the Hamiltonian is given by

$$H_0 = \sum_\mathbf{k} \epsilon^e_\mathbf{k} c^+_\mathbf{k} c_\mathbf{k} + \epsilon^h_\mathbf{k} d^+_{-\mathbf{k}} d_{-\mathbf{k}}, \tag{25}$$

where the sum over $\mathbf{k}$ is taken parallel to the heterostructure only and the subscript $_\parallel$ has been dropped for better readibility. Here, $\epsilon^e_k = E_{\text{gap}} + \hbar^2k^2/2m_e$ and $\epsilon^h_k = \hbar^2k^2/2m_h$, $m_{e/h}$ are the effective masses for the electrons/holes, respectively, and E_{gap} is the gap including the confinement energy.

To obtain a transparent description of the spatial inhomogeneities in semiconductor nanostructures close to photonic crystals, we perform a coarse graining on the length scale of an elementary cell, yielding the real-space representation

$$\hat{H}_0 = \int d^\delta r_1\left[\hat{c}^+_1\left(E_G - \frac{\hbar^2\nabla^2_1}{2m_e}\right)\hat{c}_1 + \hat{d}^+_1\left(-\frac{\hbar^2\nabla^2_1}{2m_h}\right)\hat{d}_1\right], \tag{26}$$

where the operators

$$\hat{c}^+_1(\hat{d}^+_1) = \int\frac{d^\delta k}{(2\pi)^\delta}\exp(-i\mathbf{k}\cdot\mathbf{r}_1)c^+_\mathbf{k}(d^+_\mathbf{k})$$

and $\hat{c}_1$ $(\hat{d}_1)$ create and destroy electrons of mass m_e and charge $-e$ (holes of mass m_h and charge $+e$) at $\mathbf{r}_1$, respectively, and δ is the effective dimensionality of the system.

For the light–matter interaction, we employ the dipole approximation, which is obtained by a multipole expansion over an elementary cell where only the dipole moment is taken into account. A real space representation is again obtained by a subsequent coarse graining, yielding

$$\hat{H}_I = -\int d^\delta r_1\,\mathbf{E}_1(t)\cdot\boldsymbol{\mu}(\hat{d}_1\hat{c}_1 + \hat{c}^+_1\hat{d}^+_1), \tag{27}$$

with the operator for the interband polarization $\mathbf{P}(\mathbf{r}_1, t) = \boldsymbol{\mu}(\hat{d}_1\hat{c}_1 + \hat{c}^+_1\hat{d}^+_1)$. Here, $\mathbf{E}_1(t) \equiv \mathbf{E}(\mathbf{r}_1, t)$ is the space-dependent classical electric field, $\boldsymbol{\mu}$ is the interband dipole matrix element, which is treated as a real space-independent material constant, and $\hat{d}_1\hat{c}_1$ $(\hat{c}^+_1\hat{d}^+_1)$ describes the local interband coherence, which corresponds to destroying (creating) an electron–hole pair at $\mathbf{r}_1$.

The Coulomb interaction is obtained by using $\rho(\mathbf{r}_1) = -e(c_1^+ c_1 - d_1^+ d_1)$ in Eq. (14) for the charge density. It is worthwhile to note that the Coulomb energy contains the interaction between mutually different electrons and holes as well as the self-interaction of the charge density with its own potential. While the self-interaction with the bulk part of the Coulomb potential is unphysical and can be removed by taking the normally ordered product of the field operators, the self-interaction with induced surface polarizations at the interfaces of the photonic crystal is physically meaningful and must be included.[27,28] Using the notation $V^C(\mathbf{r}_1,\mathbf{r}_2) \equiv V_{12}^C = V_{12}^0 + \delta V_{12}$ for the generalized Coulomb potential, the Coulomb Hamiltonian reads[23,26]

$$\hat{H}_C = \frac{e^2}{2}\int d^\delta r_1 \int d^\delta r_2 V_{12}^C(\hat{c}_1^+\hat{c}_2^+\hat{c}_2\hat{c}_1 + \hat{d}_1^+\hat{d}_2^+\hat{d}_2\hat{d}_1 - 2\hat{c}_1^+\hat{d}_2^+\hat{d}_2\hat{c}_1) + \frac{e^2}{2}\int d^\delta r_1 \delta V_{11}(\hat{c}_1^+\hat{c}_1 + \hat{d}_1^+\hat{d}_1). \tag{28}$$

Here, the terms in the double integral represent the repulsive electron–electron and hole–hole interactions, as well as the attractive interaction between electrons and holes. The last term of Eq. (28) describes the self-interaction of the electron and hole with their respective image charges. The self-energy $(e^2/2)\delta V_{11}$ acts as a spatially varying single-particle potential for the electrons and holes. One could thus add the terms involving $(e^2/2)\delta V_{11}$ to H_0 and solve the resulting single-particle Hamiltonian by calculating Bloch-type electronic eigenfunctions using the spatial periodicity corresponding to the period of the photonic crystal, see Sec. II D 2. Due to the very different length scales involved, i.e., the long wavelength of light and the small lattice constant, numerical evaluations of this Bloch approach are rather demanding. Nevertheless, this approach can be used to analyze the density-dependent optical absorption in quasi-equilibrium situations.[26,33]

D. Equations of motion

The dynamical properties of the semiconductor system are described by the Heisenberg equations for the relevant quantities describing the material excitations.[13] The equation of motion for the expectation value of an arbitrary operator $\mathcal{O} = \langle\hat{\mathcal{O}}\rangle$ is obtained from

$$i\hbar\frac{\partial}{\partial t}\mathcal{O}(t) = \langle[\mathcal{O},\hat{H}]\rangle. \tag{29}$$

Whereas the commutators with $\hat{H}_0$ and $\hat{H}_I$ lead to a set of closed equations of motion on the single-particle level, i.e., optical Bloch equations, the many-particle part of the Hamiltonian, $\hat{H}_C$, introduces coupling to an infinite hierarchy of correlation functions.[13,14,40] To be able to analyze the optical properties of a spatially inhomogeneous system within reasonable numerical limits, we restrict our present analysis to the level of the time-dependent Hartree–Fock approximation.[13]

As an example, we discuss the dynamics of the off-diagonal interband coherence $p_{12} = \langle\hat{p}_{12}\rangle = \langle\hat{d}_1\hat{c}_2\rangle$. Considering the contribution of the Colulomb interaction to the time derivative of the interband coherence we obtain

$$\begin{aligned} i\hbar\frac{\partial}{\partial t}\, p_{12}\big|_C &= \langle[\hat{p}_{12},\hat{H}_C]\rangle \\ &= e^2\left(\frac{1}{2}\delta V_{11} + \frac{1}{2}\delta V_{22} - V_{12}^C\right)p_{12} \\ &\quad + e^2\int d^\delta r_3 (V_{32}^C - V_{13}^C)(\langle c_3^+ d_1 c_2 c_3\rangle + \langle d_3^+ d_1 d_3 c_2\rangle). \end{aligned} \tag{30}$$

As a consequence of the many-body Coulomb interactions, we find on the right-hand side of Eq. (30) a coupling to four-operator expectation values, which is the beginning of the usual infinite hierarchy problem of many-body physics.[13,14,40] A closed set of equations is obtained by using the time-dependent Hartree–Fock factorization, which approximates the four-operator expectation values by products of two-operator expectation values.[13,14,40] This means that the four-operator terms appearing in Eq. (30) are approximated by

$$\begin{aligned} \langle c_3^+ d_1 c_2 c_3\rangle &\approx \langle c_3^+ c_3\rangle\langle d_1 c_2\rangle - \langle c_3^+ c_2\rangle\langle d_1 c_3\rangle = n_{33}^e p_{12} - n_{32}^e p_{13}, \\ \langle d_3^+ d_1 d_3 c_2\rangle &\approx \langle d_3^+ d_1\rangle\langle d_3 c_2\rangle - \langle d_3^+ d_3\rangle\langle d_1 c_2\rangle = n_{31}^h p_{32} - n_{33}^h p_{12}, \end{aligned} \tag{31}$$

where the electron (hole) populations and intraband coherences $n_{12}^e = \langle\hat{c}_1^+ c_2\rangle$ $(n_{12}^h = \langle\hat{d}_1^+ d_2\rangle)$ have been introduced.

Using such factorizations also in the equations of motion for n^e and n^h and evaluating the remaining commutators with $\hat{H}_0$ and $\hat{H}_I$, we obtain a closed set of coupled equations of motion determining the dynamics of the expectation values of all two-operator quantities. These equations are known as the SBE in time-dependent Hartree–Fock approximation.[13] For our inhomogeneous system the explicit form of the SBE is

$$\begin{aligned} i\hbar\frac{\partial}{\partial t}p_{12} &= \Bigg[E_G - \frac{\hbar^2}{2m_h}\boldsymbol{\nabla}_1^2 - \frac{\hbar^2}{2m_e}\boldsymbol{\nabla}_2^2 + \frac{e^2}{2}\delta V_{11} + \frac{e^2}{2}\delta V_{22} - V_{12}^C \\ &\quad - e^2\int d^\delta r_3 (V_{13}^C - V_{32}^C)(n_{33}^e - n_{33}^h)\Bigg]p_{12} \\ &\quad + e^2\int d^\delta r_3 (V_{13}^C - V_{32}^C)(n_{32}^e p_{13} - n_{31}^h p_{32}) \\ &\quad - \boldsymbol{\mu}\cdot(\mathbf{E}_1\delta_{12} - \mathbf{E}_1 n_{12}^e - \mathbf{E}_2 n_{21}^h) + i\hbar\frac{\partial}{\partial t}\, p_{12}\big|_{\text{corr}}, \end{aligned} \tag{32}$$

$$
\begin{aligned}
i\hbar\frac{\partial}{\partial t}n^{e}_{12} = \Bigg[& \frac{\hbar^2}{2m_e}(\boldsymbol{\nabla}_1^2-\boldsymbol{\nabla}_2^2) - \frac{e^2}{2}\delta V_{11} + \frac{e^2}{2}\delta V_{22} \\
& - e^2\int d^{\delta}r_3 (V^C_{13}-V^C_{32})(n^e_{33}-n^h_{33})\Bigg] n^e_{12} \\
& + e^2\int d^{\delta}r_3 (V^C_{13}-V^C_{32})(n^e_{13}n^e_{32}+p^{*}_{31}p_{32}) \\
& + \boldsymbol{\mu}\cdot(\mathbf{E}_1 p_{12}-\mathbf{E}_2 p^{*}_{21}) + i\hbar\frac{\partial}{\partial t}\, n^e_{12}\big|_{\text{corr}}, \qquad (33)
\end{aligned}
$$

$$
\begin{aligned}
i\hbar\frac{\partial}{\partial t}n^{h}_{12} = \Bigg[& \frac{\hbar^2}{2m_h}(\boldsymbol{\nabla}_1^2-\boldsymbol{\nabla}_2^2) - \frac{e^2}{2}\delta V_{11} + \frac{e^2}{2}\delta V_{22} \\
& + e^2\int d^{\delta}r_3 (V^C_{13}-V^C_{32})(n^e_{33}-n^h_{33})\Bigg] n^h_{12} \\
& + e^2\int d^{\delta}r_3 (V^C_{13}-V^C_{32})(n^h_{13}n^h_{32}+p^{*}_{13}p_{23}) \\
& + \boldsymbol{\mu}\cdot(\mathbf{E}_1 p_{21}-\mathbf{E}_2 p^{*}_{12}) + i\hbar\frac{\partial}{\partial t}\, n^h_{12}\big|_{\text{corr}}. \qquad (34)
\end{aligned}
$$

In Eqs. (32)–(34), the terms denoted by $|_{\text{corr}}$ represent all many-body correlations that are beyond the time-dependent Hartree–Fock limit.[13,14,40] In the analysis presented here, these correlation terms are either neglected completely or treated at a phenomenological level.

The single-particle self-energies δV appear as potentials in the homogeneous parts of the equations of motion, Eqs. (32)–(34). For the electron–hole interband coherence p_{12}, the homogeneous part of the equation of motion is furthermore influenced by the electron–hole Coulomb attraction $-e^2V^C_{12}$, which gives rise to excitonic effects in the optical spectra. Additionally, integrals over the generalized Coulomb potential V^C and products of p's and n's appear in Eqs. (32)–(34), and all equations of motion contain sources representing the driving by the electric field.

Equations (32)–(34) together with FDTD equations for the electromagnetic field allow for a self-consistent description of the dynamical evolution of the coupled light and material system, where the field is driven by the material polarization that is in turn driven by the electric field. This set of equations may be solved for arbitrary field intensities. It contains many-body Coulomb effects and can be used to investigate high-intensity effects like, e.g., excitonic Rabi-flopping, in a self-consistent fashion. Due to the self-consistency of the solution, radiative decay processes are included automatically, yielding the correct radiative decay rates for the polarization and the carrier populations even within a semiclassical description. The only aspect a semiclassical approach cannot account for is spontaneous emission, since the source term contains the expectation value of the field only and no fluctuations.

1. Low-intensity limit

In order to eliminate density-dependent shifts of the single-particle energies and to prevent rapid dephasing and relaxation due to carrier–carrier scattering, the numerical results presented in the following are obtained using incident laser beams of weak intensities. Therefore, one can describe the light–matter coupling perturbatively and classify the material excitations according to their power in the optical field.

Let us assume that the semiconductor is in its ground state before the optical excitation, i.e., the electron and hole populations as well as the intraband and interband coherences vanish initially. In this case, the linear optical properties of a semiconductor are determined by the equation of motion for the linear electron-hole interband coherence

$$
\begin{aligned}
i\hbar\frac{\partial}{\partial t}p^{(1)}_{12} = \Bigg[& E_G - \frac{1}{2m_h}\boldsymbol{\nabla}_1^2 - \frac{1}{2m_e}\boldsymbol{\nabla}_2^2 + \frac{e^2}{2}(\delta V_{11}+\delta V_{22}) \\
& - e^2V^C_{12}\Bigg] p^{(1)}_{12} - \boldsymbol{\mu}\cdot\mathbf{E}_1\delta_{12}, \qquad (35)
\end{aligned}
$$

where the superscript (1) indicates that the optical polarization is calculated in first order in the light field. By diagonalizing the homogeneous part on the right-hand side of Eq. (35), one can obtain the energies of the excitonic resonances ϵ_X and the corresponding eigenfunctions $\Psi_X(\mathbf{r}_1,\mathbf{r}_2)$. For excitation with a homogeneous light field the oscillator strength of each excitonic state is proportional to $\mu^2|\int d^{\delta}r\Psi_X(\mathbf{r},\mathbf{r})|^2$, i.e., to the absolute square of the electron–hole overlap, since the field generates electrons and holes at the same position in space, see Eqs. (27) and (35). For an inhomogeneous excitation the spatial overlap of the polarization eigenfunctions and the light field redistributes the absorption strengths of the excitonic states.

In second order in the light field, carrier populations and coherences are generated. This process is described by

$$
\begin{aligned}
i\hbar\frac{\partial}{\partial t}n^{e(2)}_{12} = & \Bigg[\frac{\hbar^2}{2m_e}(\boldsymbol{\nabla}_1^2-\boldsymbol{\nabla}_2^2) - \frac{e^2}{2}\delta V_{11} + \frac{e^2}{2}\delta V_{22}\Bigg] n^{e(2)}_{12} \\
& + \int d^{\delta}r_3 e^2 (V^C_{13}-V^C_{32})(p^{(1)}_{31})^{*}p^{(1)}_{32} \\
& + \boldsymbol{\mu}\cdot(\mathbf{E}_1 p^{(1)}_{12} - \mathbf{E}_2 (p^{(1)}_{21})^{*}), \qquad (36)
\end{aligned}
$$

$$
\begin{aligned}
i\hbar\frac{\partial}{\partial t}n^{h(2)}_{12} = & \Bigg[\frac{\hbar^2}{2m_h}(\boldsymbol{\nabla}_1^2-\boldsymbol{\nabla}_2^2) - \frac{e^2}{2}\delta V_{11} + \frac{e^2}{2}\delta V_{22}\Bigg] n^{h(2)}_{12} \\
& + \int d^{\delta}r_3 e^2 (V^C_{13}-V^C_{32})(p^{(1)}_{13})^{*}p^{(1)}_{23} \\
& + \boldsymbol{\mu}\cdot(\mathbf{E}_1 p^{(1)}_{21} - \mathbf{E}_2 (p^{(1)}_{12})^{*}). \qquad (37)
\end{aligned}
$$

By diagonalizing the homogeneous part on the right-hand side of Eqs. (36) and (37) one can determine the electron and hole eigenstates. These can be populated according to Fermi functions and inserted into Eq. (32) if one wants to study the density-dependent absorption in quasi-equilibrium situations.[13,26,33]

Note that due to the spatial integrals which appear as a consequence of the many-body Coulomb interaction it requires a lot more effort to numerically solve Eqs. (36) and (37) than the equation for the linear polarization, Eq. (35), which contains no spatial integrals. However, if the dynamics is coherent and one considers only terms up to second order in the field, i.e., in the coherent $\chi^{(2)}$-limit, it is actually not necessary to solve the combined set of Eqs. (35)–(37). Using the equations of motion, one can easily verify that in this limit the carrier populations and intraband coherences are determined by the interband coherence via the sum rules

$$n_{12}^{e(2)} = \int d^{\delta}r_3 p_{32}^{(1)} (p_{31}^{(1)})^*, \tag{38}$$

$$n_{12}^{h(2)} = \int d^{\delta}r_3 p_{23}^{(1)} (p_{13}^{(1)})^*, \tag{39}$$

i.e., they are given by spatial integrals over products of linear polarizations.

2. Dephasing and relaxation

Due to the self-consistent solution of Maxwell's equations together with the SBE, the radiative decay of the photoexcited optical polarization and the populations is automatically included in our description. However, in real systems the material excitations often decay on shorter time scales. The coupling between the electron and the phonon system can be responsible for this, as well as the many-body correlation contributions, which include Coulomb scattering processes. Since a microscopic treatment of these processes in spatially inhomogeneous situations requires a very high numerical effort, we model them phenomenologically by inserting decay and relaxation times into the equations of motion.

The nonradiative decay of the interband polarization, often called dephasing, is assumed to be exponential and is described by adding $-i\hbar p_{12}^{(1)}/T_2^*$ to the right-hand side of Eq. (35). The total polarization decay time T_2 contains radiative and nonradiative contributions and is obtained as $T_2^{-1}=T_{\text{rad}}^{-1}+T_2^{*-1}$. In the coherent limit, the dephasing of the carrier populations and intraband coherences is induced purely by the finite lifetime of the photoexcited carriers. Thus, the carrier populations and intraband coherences decay with the time constant $T_2/2$. Since the radiative contributions are included automatically through the self-consistent solution of the MSBE only the nonradiative contributions $-i\hbar n_{12}^{e(2)}/(T_2^*/2)$ and $-i\hbar n_{12}^{h(2)}/(T_2^*/2)$ must be added to the right- hand sides of Eqs. (36) and (37). In this case, the sum rules, Eqs. (38) and (39), remain valid and thus $n_{12}^{e(2)}$ and $n_{12}^{h(2)}$ can be calculated using $p_{12}^{(1)}$.

However, in reality the coherent limit is often not well suited to describe the dynamics of the electron–hole excitations in semiconductors. Typically, the populations and intraband coherences do not vanish on a time scale similar to the dephasing of the optical polarization, but rather become incoherent and approach quasi-equilibrium distributions in the respective bands. This thermalization process can be modeled by adding $-i\hbar(n_{12}^{e(2)}-n_{12}^{e,\text{eq}})/T_1$ and $-i\hbar(n_{12}^{h(2)}-n_{12}^{h,\text{eq}})/T_1$, where $n_{12}^{e,\text{eq}}$ and $n_{12}^{h,\text{eq}}$ denote the populations and intraband coherences in quasi-thermal equilibrium, to the right-hand sides of Eqs. (36) and (37). Since in this case the sum rules, Eqs. (38) and (39), are not valid any more, the dynamics of $n_{12}^{e(2)}$ and $n_{12}^{h(2)}$ has to be determined by solving Eqs. (36) and (37) together with Eq. (35). However, also in this situation it is possible to avoid the evaluation of the space integrals in the equations of motion. This can be achieved by decomposing $n_{12}^{e(2)}$ and $n_{12}^{h(2)}$ into a coherent and an incoherent part via

$$n_{12}^{e(2)} = n_{12}^{e(2);\text{coh}} + n_{12}^{e(2);\text{incoh}}, \tag{40}$$

$$n_{12}^{h(2)} = n_{12}^{h(2);\text{coh}} + n_{12}^{h(2);\text{incoh}}. \tag{41}$$

The coherent parts of $n^{e(2)}$ and $n^{h(2)}$ are obtained using Eqs. (38) and (39), i.e., they decay with a time constant of $T_2/2$. By inserting Eqs. (40) and (41) into Eqs. (36) and (37), respectively, and subtracting the coherent parts, one can determine the following equations of motion for the incoherent terms:

$$\begin{aligned} i\hbar\frac{\partial}{\partial t} n_{12}^{e(2);\text{incoh}} &= \left[\frac{\hbar^2}{2m_e}(\boldsymbol{\nabla}_1^2-\boldsymbol{\nabla}_2^2) - \frac{e^2}{2}\delta V_{11} + \frac{e^2}{2}\delta V_{22}\right] n_{12}^{e(2);\text{incoh}} \\ &\quad - i\hbar n_{12}^{e(2);\text{coh}}\left(\frac{1}{T_1}-\frac{1}{T_2^*/2}\right) - i\hbar\frac{n_{12}^{e(2);\text{incoh}}-n_{12}^{e,\text{eq}}}{T_1}, \end{aligned} \tag{42}$$

$$\begin{aligned} i\hbar\frac{\partial}{\partial t} n_{12}^{h(2);\text{incoh}} &= \left[\frac{\hbar^2}{2m_h}(\boldsymbol{\nabla}_1^2-\boldsymbol{\nabla}_2^2) - \frac{e^2}{2}\delta V_{11} + \frac{e^2}{2}\delta V_{22}\right] n_{12}^{h(2);\text{incoh}} \\ &\quad - i\hbar n_{12}^{h(2);\text{coh}}\left(\frac{1}{T_1}-\frac{1}{T_2^*/2}\right) \\ &\quad - i\hbar\frac{n_{12}^{h(2);\text{incoh}}-n_{12}^{h,\text{eq}}}{T_1}. \end{aligned} \tag{43}$$

Equations (42) and (43) show that the incoherent populations and intraband coherences have two sources. If $T_1 \neq T_2^*/2$ they are generated directly from the coherent terms. Furthermore, the relaxation toward quasi-equilibrium distributions always leads to incoherent terms, since $n^{e,\text{eq}}$ and $n^{h,\text{eq}}$ are determined by the total (coherent and incoherent) populations, see the following.

In order to determine the quasi-equilibrium distributions, first the effective single-particle Hamiltonian defined by

$$\begin{aligned} \hat{H}_{\text{single-particle}} &= \hat{H}_{\text{band structure}} + \hat{H}_{\text{Coulomb self-energies}} \\ &= \int d^{\delta}r_1 \left[\hat{c}_1^+\left(E_G - \frac{\hbar^2\boldsymbol{\nabla}_1^2}{2m_e}\right)\hat{c}_1 + \hat{d}_1^+\left(-\frac{\hbar^2\boldsymbol{\nabla}_1^2}{2m_h}\right)\hat{d}_1\right] \\ &\quad + \frac{1}{2}\int d^{\delta}r_1 \delta V_{11}(\hat{c}_1^+\hat{c}_1 + \hat{d}_1^+\hat{d}_1) \end{aligned} \tag{44}$$

is diagonalized. Note that, besides the kinetic energies also the spatially varying self-energies, which act as inhomogeneous potentials, are included in Eq. (44). By diagonalizing this Hamiltonian separately for electrons and holes using the spatial periodicity induced by the photonic crystal, the dispersions $\epsilon_{\mathbf{k}}^{\nu}$, where ν labels the mini-bands, and the corresponding Bloch-type eigenfunctions $\Phi_{\mathbf{k}}^{\nu}(\mathbf{r})$ are obtained. Since in the situations analyzed in the following the spatial period is relatively large, sufficiently many (about 100 in the one-dimensional situation considered here) of the energetically rather narrow mini-bands have to be included in the calculation.

In this single-particle basis, the states are populated according to a quasi-equilibrium distribution, i.e., $n_{\mathbf{k}}^{\nu}$ is given by the Fermi function F. The total density n at temperature T can be expressed as

$$n = \sum_{\mathbf{k},\nu} n_{\mathbf{k}}^{\nu} = \sum_{\mathbf{k},\nu} F(\epsilon_{\mathbf{k}}^{\nu}, T, \mu), \tag{45}$$

where $n_{\mathbf{k}}^{\nu}$ denotes the population of state $\Phi_{\mathbf{k}}^{\nu}$ with energy $\epsilon_{\mathbf{k}}^{\nu}$. Since the total density n depends on the chemical potential, μ needs to be determined self-consistently. Having obtained $n_{\mathbf{k}}^{\nu}$, we then transform back to real space since this is numerically advantageous for performing the dynamic calculations. In the time-dependent solutions of the equations of motion the carrier density is changing during the optical excitation. Therefore, the numerically calculated time-dependent density $n(t)$ is used to determine the quasi-equilibrium $n_{12}^{e,\text{eq}}(t)$ and $n_{12}^{e,\text{eq}}(t)$ real-space populations and intraband coherences.

III. NUMERICAL RESULTS

A. Semiconductor photonic-crystal structure

Numerical solutions of the MSBE for semiconductor photonic-crystal structures typically require a considerable amount of computer time and memory. On the one hand, in general situations a three-dimensional space discretization is necessary for FDTD solutions of Maxwell's equations. Since the optical wavelength and the photonic structure have to be resolved with a suitable accuracy, such evaluations have to be performed with a high number of grid points. On the other hand, due to the generalized Coulomb interaction and the coupling to spatially inhomogeneous light fields, the analysis of the material excitations has to be performed taking into account both the relative and the center-of-mass coordinates. Thus the SBE have to be solved for a spatially inhomogeneous situation where different length scales have to be resolved since typically the exciton Bohr radius is about one order of magnitude smaller than the optical wavelength.

In order to keep these numerical complexities within reasonable limits, we chose for the analysis presented in this paper a model system consisting of a one-dimensional array of dielectric slabs ($\epsilon=13$) which extend in z direction and are separated by air ($\epsilon=1$), see Fig. 1. The substrate below this dielectric structure is made of the same material as the dielectric slabs. Light propagating in this structure may create photoexcitation in an array of parallel semiconductor quantum wires, which extend in y direction perpendicular to the slabs and are separated from the photonic structure by the distance S. In y direction the unit cell with length L is repeated periodically. In addition, periodic boundary conditions are also used in z direction with period D, which is the distance between adjacent quantum wires. The parameters used in the numerical calculations are as follows: the length of the unit cell in y direction is $L=180$ nm, the height of the slabs is $H=700$ nm, and for the width W of the slabs different values are used. The parallel wires are separated by $D=30$ nm and the distance to the photonic crystal is $S=2.6$ nm. This value is assumed to be small in order to obtain a significant modification of the Coulomb interaction in the quantum wires.

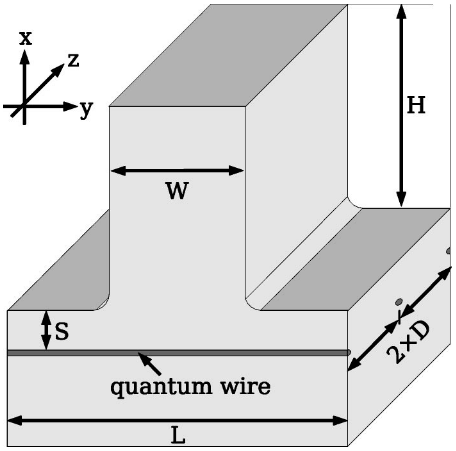

FIG. 1. Schematical drawing of the considered semiconductor photonic-crystal structure. The photonic crystal is a periodic one-dimensional array of dielectric slabs ($\epsilon=13$) which are separated by air ($\epsilon=1$). The length L of the unit cell in y direction is 180 nm. The substrate below the photonic crystal is made of the same material as the dielectric slabs. It surrounds the array of parallel quantum wires which lies $S=2.6$ nm underneath the photonic crystal. The distance between adjacent wires, which is also the length of the unit cell in z direction, is $D=30$ nm. For the width W of the slabs we use values of 0, 60, 90, 120, and 180 nm, respectively. The situations $W=0$ and $W=L=180$ nm are denoted by half-space and homogeneous case, respectively, as explained in the text. The height H of the slabs is always 700 nm.

Due to the light propagation through the dielectric structure, the optical field is spatially inhomogeneous at the positions of the quantum wires. Furthermore, since the wires are oriented perpendicular to the dielectric slabs, the generalized Coulomb interaction varies periodically along the wires. Our model system thus includes both a space-dependence of the electromagnetic field and space-dependent modifications of the semiconductor properties.

For later purposes, we introduce two reference systems. The limit $W=L$ is referred to as the homogeneous case, since the dielectric–air interface is far away ($S+H=702.6$ nm) from the semiconductor quantum wires and thus the modifications of the Coulomb interaction are negligible. In the second limit $W=0$, which is denoted as the half-space case, the planar air–dielectric interface is very close ($S=2.6$ nm) to the semiconductor wire array. Therefore, the Coulomb interaction is significantly modified. Due to the planar interfaces, the generalized Coulomb potential is homogeneous with respect to the center-of-mass coordinate along the quantum wire for both limiting cases.

In our calculations, we solve Eq. (18) for a single dielectric slab, insert the solution in Eq. (16) to obtain the modified Coulomb interaction, and add the resulting δV for the two nearest slabs neglecting the surface polarizations between them. Numerical tests have justified this approximation if the distance between the slabs is not too small. The edges between the dielectric substrate and the slabs have been smoothed as shown in Fig. 1. This avoids numerical problems when solving Eq. (18) using the Nystrom method and takes into account that realistic photonic crystals made by etching techniques have no sharp edges.

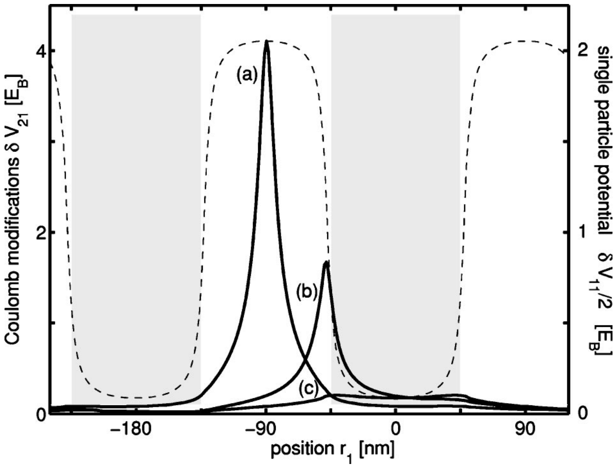

FIG. 2. Modification of the Coulomb potential $\delta V(\mathbf{r}_2,\mathbf{r}_1)=\delta V_{21}$ (solid) in the quantum wires for positions $r_2=-90$ nm (a), $r_2=-45$ nm (b), and $r_2=0$ nm (c) as function of position r_1. The single-particle potential $\delta V(\mathbf{r}_1,\mathbf{r}_1)/2=\delta V_{11}/2$ is also displayed (dashed). The dielectric slabs of the photonic crystal are $W=90$ nm wide and $H=700$ nm high. Positions r_1 underneath the slabs are indicated by the gray areas. The energy unit is the three-dimensional exciton binding energy of GaAs $E_B=4.25$ meV.

Figure 2 shows the Coulomb modifications $\delta V(r_2,r_1)$ in the quantum wires for three fixed, representative positions $r_2=-90$ nm (a), $r_2=-45$ nm (b), and $r_2=0$ nm (c) as function of position r_1. Positions r_1 underneath the 90-nm-wide dielectric slabs are indicated by the gray shading. The Coulomb modifications δV are small for positions r_2 directly underneath the slabs, like in case (c), since in this situation the distance to the dielectric–air interfaces of the photonic structure is large. δV is bigger in the regions between the slabs, as can be seen in case (a), because in this situation the distance to the dielectric–air interfaces is small. Between these extremal values, there is a quite sharp transition which takes place within a few nanometers directly under the edges of the slabs, i.e., at ±45 nm in Fig. 2. The single-particle potential $\delta V(r_1,r_1)/2$, dashed line in Fig. 2, shows this sharp transition and follows the periodicity of the photonic crystal. For short distances $|r_1-r_2|$, the magnitude and space dependence of the modified Coulomb interaction calculated for $r_2=-90$ nm, i.e., case (a) in Fig. 2, differ only marginally from those which arise for the half-space case ($W=0$). The curves (a) and (b) show a strong decrease of the Coulomb modifications with increasing distance between r_1 and r_2. For particle positions r_2 underneath the slab, i.e., case (c), δV depends only weakly on distance for distances smaller than the half slab width, and decreases significantly if the distance exceeds $W/2$.

Figure 2 shows that the spatially periodically varying dielectric environment introduces a periodic single particle potential for the electron and holes, with minima underneath the dielectric slabs. This single particle potential influences the optical and electronical properties of the quantum wire via electron and hole confinement effects and a periodic modulation of the effective band gap. Furthermore, excitonic properties are additionally altered as a result of the modified space-dependent electron-hole attraction. All these effects are analyzed in the following.

B. Linear excitonic absorption

In this section, the excitonic resonances in the linear absorption spectra are obtained by solving the linear polarization equation, Eq. (35). We assume the incoming external light field to be a plane wave propagating in negative x direction. The incident electric field is linearly polarized in y direction, i.e., in the direction of the quantum wires. The y and z components of the electric and magnetic field, E_y and H_z, respectively, have slowly varying Gaussian envelopes and oscillate in time with central frequencies close to the band gap frequency, i.e., $E_G/\hbar$. The linear spectra, which are analyzed below, have been computed using the net energy flux through the boundaries of our FDTD simulation space

$$\Delta\dot{E}=\int d\sigma\mathbf{n}\cdot\mathbf{S}, \tag{46}$$

where $\mathbf{S}=\mathbf{E}\times\mathbf{H}$ is the Poynting vector. The net flux contains all information about the absorbed or gained energy per unit time. In spectrally resolved experiments, the net flux is measured over all times and analyzed in frequency space

$$\Delta E=\int dt\,\Delta\dot{E}=\int d\omega\alpha(\omega)I_0(\omega), \tag{47}$$

where

$$\alpha(\omega)=\frac{1}{I_0}\int d\sigma(\mathbf{E}^*(\mathbf{r},\omega)\times\mathbf{H}(\mathbf{r},\omega)+\text{c.c.})\cdot\mathbf{n}, \tag{48}$$

and $I_0(\omega)$ is the intensity of the incoming light field. The absorption spectra shown in the following have been obtained by computing $\alpha(\omega)$ from Eq. (48).

The semiconductor parameters used in the following are $\boldsymbol{\mu}=3.5\,e\text{Å}\mathbf{e}_y$ for the dipole matrix element, $m_h/m_e=4$ and $m_e=0.066m_0$ for the electron and hole masses, and $E_G=1.42$ eV for the energy gap. Considering a dielectric constant of $\boldsymbol{\epsilon}=13$, these parameters result in a three-dimensional exciton binding energy of $E_B=4.25$ meV and a Bohr radius of $a_B\approx 13$ nm. In most of the calculations, nonradiative homogeneous broadening is modeled by introducing a decay rate of $\gamma=\hbar/T_2^*=1$ meV in the equation of motion of the interband polarization. The Coulomb potential for the one-dimensional wires has been regularized using $V_0=1/(|r|+a_0)$.[41,42] The regularization parameter is chosen as $a_0=0.16\,a_B$. Except for changes of the nonradiative decay time T_2^* in Secs. III C and III D, these parameters are kept constant in the following. Additionally, we consider dielectric slabs with a thickness of $W=90$ nm, except in Fig. 3 where the influence of W on the excitonic absorption is investigated.

To obtain the results presented in the following, the FDTD calculations are performed on a grid with a spatial resolution of 5 nm, which requires a temporal resolution of $dt=dx/(2c)\simeq 8.3\times 10^{-18}$ s.[31] The SBE have to be solved with a resolution smaller than the exciton Bohr radius a_B. Therefore, we use here 1.3 nm, i.e., $\approx a_B/10$. The self-consistent solution of the MSBE is done in the following scheme: With the electric field at time t, the magnetic field at $t+dt/2$ and the polarization at $t+dt$ are computed. The po-

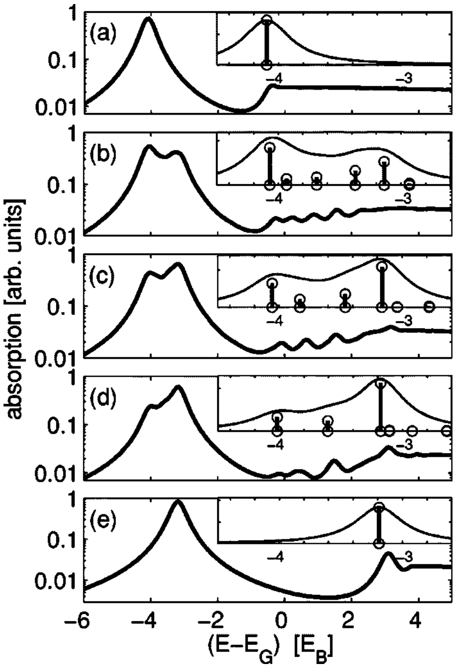

FIG. 3. Excitonic linear absorption spectra for dielectric slabs of widths $W=180$ nm (a), $W=120$ nm (b), $W=90$ nm (c), $W=60$ nm (d), and $W=0$ nm (e), respectively, on a logarithmic scale. The height of the slabs is 700 nm in all cases. The insets show the decomposition of the excitonic resonances into the contributing bound excitonic states and their oscillator strengths on a linear scale: (a) corresponds to the homogeneous case and (e) to the half-space case. The calculations have been performed using a damping of $\gamma=1$ meV for the interband polarization and a quantum wire length of five unit cells with periodic boundary conditions.

larizations at t and $t+dt$ are used to determine its time derivative at $t+dt/2$ which together with the magnetic field allows us to evaluate the electric field at $t+dt$. Then these steps are repeated.

For the case of a semiconductor quantum well placed close to a planar dielectric–air interface, image charge effects cause a shift of the single-particle energies, i.e., the band gap shifts to higher energies. Since the electron–hole attraction is increased close to air, the exciton binding energy increases as well.[23,28] In semiconductor photonic-crystal structures both the band gap and excitonic binding energy become space dependent.[24,25] The band gap variation induces potential valleys underneath the dielectric slabs which give rise to confined single-particle and exciton states, see insets in Fig. 3. These local potentials affect the linear absorption spectra and cause the double-peaked 1*s*-exciton resonance visible in Figs. 3(b)–3(d). Note that the spectra are plotted on a logarithmic scale which emphasizes the continuum absorption. For comparison, also the homogeneous and the half-space cases are shown in Figs. 3(a) and 3(e), respectively. Figure 3 demonstrates that the spectral positions of the two excitonic peaks are hardly affected by varying the width of the dielectric slabs. Whereas the lower exciton energy agrees with the position of the exciton in the homogeneous case, the upper one corresponds to the half-space case. In contrast to the energetic positions, the heights of the maxima are influenced significantly by the width of the dielectric slabs. With decreasing width, the absorption of the lower homogeneous-like peak becomes smaller while that of the upper half-space-like peak increases.

Further information on the relevant exciton resonances is shown in the insets of Fig. 3. Diagonalizing the linear polarization equation, Eq. (35), for one unit cell with periodic boundary conditions yields the energetic positions of the excitonic states. Since the optical field at the quantum wire is spatially varying, the oscillator strengths of the different resonances have been computed by fitting the self-consistently evaluated linear absorption spectra by a sum of Lorentzian curves $\Sigma_i A_i/((E-\epsilon_{X,i})^2+\gamma^2)$, where $\gamma=1$ meV is the decay constant used in the equation of motion for the interband polarization. The insets of Fig. 3 show that except for the homogeneous and the half-space cases, which are dominated by a single excitonic peak, more than two excitonic resonances contribute to the absorption. However, for all considered widths of the dielectric slabs the two most strongly absorbing resonances are at the energetic positions of the homogeneous and the half-space excitons.

The number of quantized exciton states is determined by the width of the dielectric slabs. For a 180-nm-wide slab, i.e., in the homogeneous case, the Coulomb modifications essentially vanish and only the homogeneous 1*s*-exciton resonance contributes, see Fig. 3(a). For slab widths in between 180 and 0 nm potential valleys appear, see Fig. 2. The maxima and minima of the space-dependent potential lie between the values of the half-space and the homogeneous case. The potential valleys are deepest for intermediate slab widths, i.e, for $W=90$ nm$=L/2$. Correspondingly, Figs. 3(a)–3(e) nicely reflect the transition from the homogeneous to the half-space case which takes place with decreasing slab width.

The logarithmic plots of the linear absorption show that the band gap appears at 0 E_B and ≈ 4 E_B for the homogeneous and the half-space case, respectively, see Figs. 3(a) and 3(e). Thus the exciton binding energy, i.e., the energetic distance between the lowest exciton resonance and the onset of the continuum, increases from 4 E_B in the homogeneous case to ≈ 7.2 E_B in the half-space case. Qualitatively similar results have been obtained for quantum wells close to two-dimensional photonic crystals.[24,25] In Figs. 3(a) and 3(e), the 2*s*-exciton resonances are visible as small peaks at ≈ -0.5 E_B and ≈ 3.1 E_B. For energies above ≈ 3.4 E_B the continuum absorption is smooth also for the spatially inhomogeneous cases, Figs. 3(b)–3(d). The inhomogeneity of the system causes the appearance of small absorption peaks in between ≈ -0.5 E_B and ≈ 3.1 E_B which can be viewed as modified higher excitonic resonances.

For a more detailed understanding of the excitonic resonances, we show in Fig. 4 also the polarization eigenfunctions, which belong to the excitonic states of Fig. 3(c). These polarization eigenfunctions $\Psi_X(r_1,r_2)$ have been obtained by diagonalization Eq. (35) and are real, since we use one unit cell with periodic boundary conditions. Shown in Fig. 4(b) is the spatial variation of the eigenfunction for equal electron and hole positions, i.e., $\Psi_X(r_1,r_1)$. The three lowest states are localized in the potential valley underneath the dielectric slabs, see Figs. 4(b) and 4(c). They look similar to usual

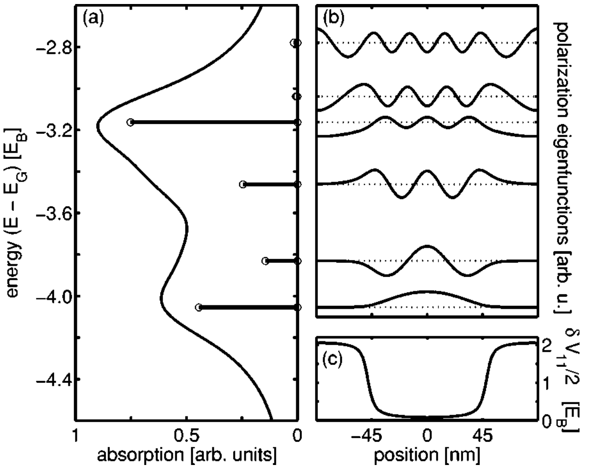

FIG. 4. (a) Linear excitonic absorption spectrum for the parameters considered in Fig. 3(c). The lines indicate the spectral positions and the oscillator strengths of the contributing excitonic resonances. (b) Eigenfunctions of the interband polarization obtained by diagonalizing Eq. (35). Shown is the spatial variation of the polarization eigenfunction for equal electron and hole positions, i.e., $\Psi_{X,i}(r_1,r_1)$. The dotted lines indicate the eigenenergies $\epsilon_{X,i}$ and correspond to the zero polarization axes. (c) Corresponding single-particle potential induced by the spatially-varying dielectric environment.

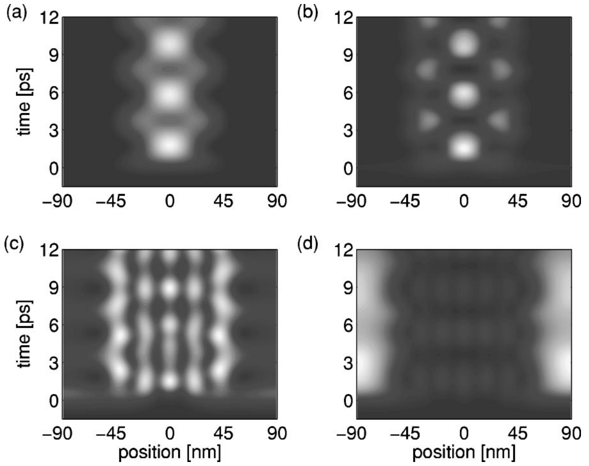

FIG. 5. Contour plots showing the spatiotemporal dynamics of the coherent electron density $n_{11}^{e(2);\mathrm{coh}}$, see Eq. (38), along one quantum wire unit cell. The system is excited by a Gaussian pulses of 2 ps duration (FWHM). The central frequencies of the pulses, ω_L, are tuned to the four lowest exciton states: (a) $\hbar\omega_L = E_G - 4.05\ E_B$, (b) $\hbar\omega_L = E_G - 3.83\ E_B$, (c) $\hbar\omega_L = E_G - 3.46\ E_B$, and (d) $\hbar\omega_L = E_G - 3.16\ E_B$, respectively. The dielectric slabs are $W = 90$ nm wide and $H = 700$ nm high. The calculations have been performed assuming a fully coherent situation, i.e., nonradiative dephasing and thermalization have not been considered $(T_1, T_2^* \rightarrow \infty)$. White corresponds to the maximal density and black to zero density in each plot.

quantum mechanical eigenfunctions of a particle which is confined in a box-shaped potential and show an increasing number of nodes with increasing energy. Due to its higher energy, the fourth state has strong contributions for positions in between the dielectric slabs, which explains its half-space like character. The energetically higher fifth and sixth states contribute negligibly to the excitonic absorption.

When diagonalizing Eq. (35), we obtain also polarization eigenfunctions which are antisymmetric, i.e., $\Psi_X(r_1,r_1) = -\Psi_X(-r_1,-r_1)$. Because of our initial conditions for the light field these antisymmetric solutions of the polarization are not excited and do not contribute to the absorption. This is due to the fact that the incident light field is a homogeneous plane wave which propagates in negative x direction. The photonic crystal destroys the spatial homogeneity of the field but maintains its mirror symmetry with respect to the middle of one unit cell. Therefore, the overlap between the symmetric light field and an antisymmetric wave function vanishes. For a spatially structured incident light field or propagation in a different direction, the symmetry of the system is broken and the antisymmetric wave function can be excited.

C. Coherent wave packet dynamics

So far, we have focused on the linear optical properties of the system, e.g., the excitonic resonances, their oscillator strengths, resonance energies, and space-dependent eigenfunctions. In this section we start to investigate the intricate coherent wave packet dynamics of the electron density after resonant excitation of the excitonic resonances. The absorption spectra shown in the previous section have been computed using five unit cells for the quantum wire with periodic boundary conditions. This number of unit cells is required to obtain a converged continuum absorption. The exciton resonances are, however, already stable for just one unit cell. Therefore, it is justified to reduce the numerical requirements for the following investigations by considering one unit cell with periodic boundary conditions.

The densities are calculated for excitation with laser pulses of weak intensities up to second order $(\chi^{(2)})$ in the light–matter interaction. In this section, we focus on the fully coherent dynamics and neglect nonradiative dephasing and relaxation processes, i.e., the limit T_1, $T_2^* \rightarrow \infty$. The coherent electron density is obtained by solving Eq. (35) and using Eq. (38). Figure 5 shows the spatiotemporal dynamics of the electron density $n_{11}^{e(2);\mathrm{coh}}$ after excitation with a Gaussian pulse of 2 ps full width at half maximum (FWHM) duration of the pulse envelope and a central frequency which is tuned to the four energetically lowest excitonic resonances shown in Fig. 4. For excitation at the three lowest resonances, Figs. 5(a)–5(c), the electron density is basically concentrated at spatial positions underneath the dielectric slabs, i.e., between ±45 nm. Since the spectral width of the incident electric field of 0.3 E_B (FWHM of field intensity) is comparable to the energetic spacing between the resonances, the density is not constant as function of time. The pulses generate a coherent superposition of the exciton transitions which leads to wave packet dynamics. However, comparing Figs. 5(a)–5(c) with the electron densities corresponding to the three lowest resonances, see Fig. 6, shows that the resonantly excited excitons give the strongest contributions to the density. When exciting at the fourth excitonic resonance, Fig. 5(d), the electron den-

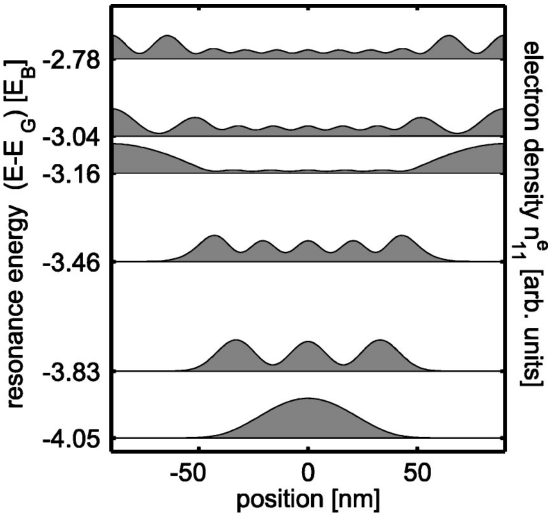

FIG. 6. Coherent electron densities calculated using Eq. (38) and the polarization eigenfunctions shown in Fig. 4(b). On the left side the energetic positions of the resonances are shown. The vertically displaced lines indicate zero density.

sity is concentrated underneath the air regions of the photonic crystal. In this case the density dynamics corresponds essentially to a coherent superposition of the fourth and third excitonic resonances, see Fig. 6.

By using spectrally narrower, i.e., temporally longer laser pulses, it is possible to selectively excite single exciton resonances. In this case the coherently excited electron density is constant as function of time and shows a spatial profile corresponding to the curves shown in Fig. 6. As an example, we consider in Fig. 7 the excitation with a Gaussian pulses which are tuned to the third lowest exciton state and have different temporal durations. The short 1 ps pulse, Fig. 7(a), generates essentially a superposition of the four lowest excitonic resonances. Consequently, the wave packet dynamics shows a complicated pattern and the density covers all spatial positions. For the 2 ps pulse, Fig. 7(b), the time evolution is basically dominated by the third and fourth excitonic states since their energetic separation is smaller than the energy difference between the third and the second states. The influence of the fourth state is reduced when the pulse duration is increased to 2.5 ps. Finally, for a 4.5 ps pulse the coherently excited density shows no dynamics but just a fixed shape which is determined by the wave function of the third exciton resonance, cf. Fig. 6.

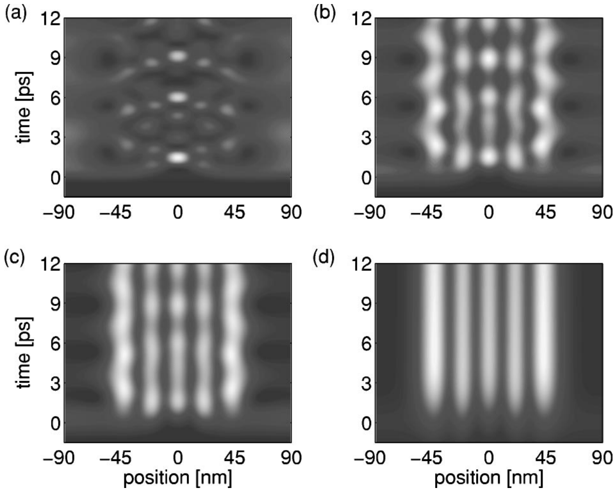

FIG. 7. Contour plots showing the spatiotemporal dynamics of the coherent electron density $n_{11}^{e(2);\mathrm{coh}}$, see Eq. (38), along one quantum wire unit cell. The system is excited by Gaussian pulses of 1 ps (a), 2 ps (b), 2.5 ps (c), and 4.5 ps (d) duration (FWHM), respectively. The central laser frequency has been tuned to the third exciton resonance $\hbar\omega_L = E_G - 3.46\ E_B$. The dielectric slabs are $W = 90$ nm wide and $H = 700$ nm high. The calculations have been performed assuming a fully coherent situation, i.e., nonradiative dephasing and thermalization have not been considered $(T_1, T_2^* \rightarrow \infty)$. White corresponds to the maximal density and black to zero density in each plot.

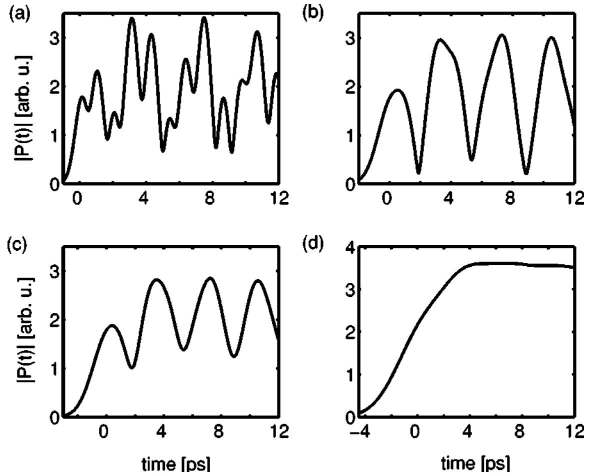

FIG. 8. Temporal dynamics of the modulus of the spatially integrated macroscopic optical polarization for resonant excitation of the third exciton, i.e., $\hbar\omega_L = E_G - 3.46\ E_B$, using Gaussian laser pulses of durations of 1 ps (a), 2 ps (b), 2.5 ps (c), and 4.5 ps (d) (FWHM), respectively. The system parameter are the same as in Fig. 7.

A similar analysis can be performed by monitoring the time dependence of the spatially integrated optical polarization for different widths of the incident laser pulses. The modulus of the polarization when exciting with a 1 ps pulse, Fig. 8(a), shows modulations with a few frequencies. For the 2 ps pulse, Fig. 8(b), and more clearly for the 2.5 ps pulse, Fig. 8(c), the modulations are dominated by a single frequency, i.e., in these cases only two excitonic transitions contribute strongly to the polarization. For the long 4.5 ps pulse, Fig. 8(d), only a single exciton resonance contributes and consequently the polarization shows no modulations as function of time. Note that the very slow decay of the polarization is due to the radiative decay which is included in our self-consistent solutions of the MSBE.

Such investigations have also been performed for the holes. The results are qualitatively similar to the ones obtained for the electrons. However, due to the bigger effective mass of the holes they are more strongly confined in the potential valley and therefore their density shows somewhat more pronounced maxima and minima.

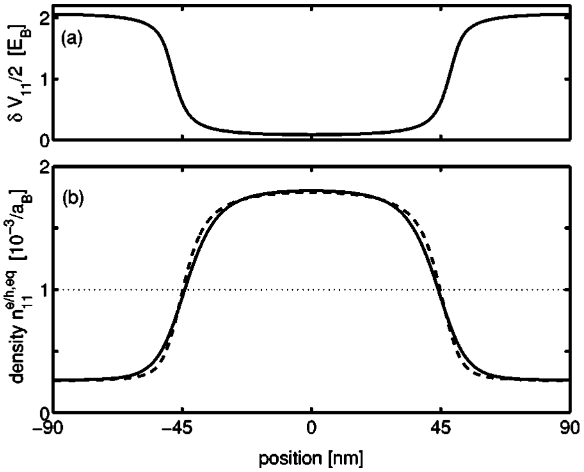

FIG. 9. (a) Single-particle potential $\delta V_{11}/2$ and (b) space-dependent quasi-equilibrium electron (solid) and hole (dashed) carrier densities, i.e., $n_{11}^{e/h;\text{eq}}$, for an average density of $n_0=0.001/a_B$ (dotted) at a temperature of 50 K. The width of the dielectric slabs is 90 nm.

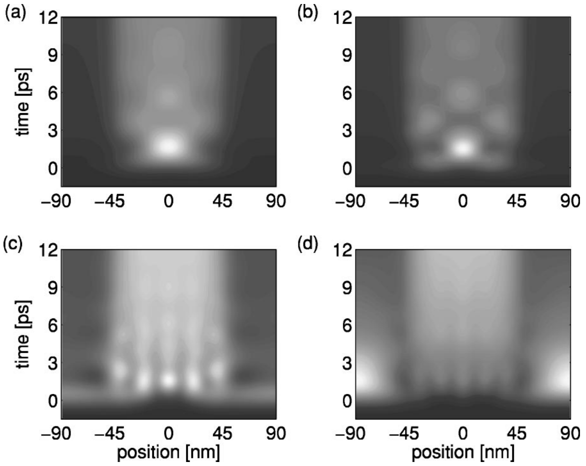

FIG. 10. Contour plots showing the spatiotemporal dynamics of the coherent electron density $n_{11}^{e(2)}$, see Eq. (40), along one quantum wire unit cell. The system is excited by a Gaussian pulses of 2 ps duration (FWHM). The central frequencies of the pulses, ω_L, are tuned to the four lowest exciton states: (a) $\hbar\omega_L=E_G-4.05\ E_B$, (b) $\hbar\omega_L=E_G-3.83\ E_B$, (c) $\hbar\omega_L=E_G-3.46\ E_B$, and (d) $\hbar\omega_L=E_G-3.16\ E_B$, respectively. The dielectric slabs are $W=90$ nm wide and $H=700$ nm high. Nonradiative dephasing and relaxation processes have been included using $T_1=T_2^*=6$ ps at a temperature of 50 K. Except for the dephasing and relaxation, the material parameters and the excitation conditions are the same as in Fig. 5. White corresponds to the maximal density and black to zero density in each plot.

D. Wave packet dynamics with dephasing and relaxation

Exciting semiconductor heterostructures with a short optical laser pulse produces a coherent optical polarization in the material. With increasing time this polarization decays due to a variety of dephasing processes. Depending on the relevant physical mechanisms and the excitation conditions, typical dephasing times can vary between several picoseconds or just a few femtoseconds. Radiative decay due to the finite lifetime of the excited states always contributes to the decay of the optical polarization. However, in semiconductors the dephasing is typically dominated by the interaction with phonons, by the many-body Coulomb interaction, or sometimes by disorder.[43] Simultaneous with the dephasing of the polarization, the initially coherently excited carrier distributions change their nature and gradually become incoherent. Due to the interaction with phonons and Coulomb scattering among the electrons and holes, these incoherent populations approach thermal quasi-equilibrium distributions with increasing time.

For spatially homogeneous systems, it is possible to describe dephasing and relaxation at a microscopic level.[13,43] For spatially inhomogeneous systems such an analysis is much more complicated. For example, the evaluation of Coulomb scattering processes in the presence of disorder are computationally very demanding and can be performed only for very small systems, see, e.g., Ref. 44. Therefore, we describe these processes here on a phenomenological level. As outlined in Sec. II D 2, the nonradiative decay of the polarization is modeled by a dephasing time T_2^* and the carrier populations approach a quasi-equilibrium Fermi–Dirac distribution within the relaxation time T_1.

Figure 9(b) shows the electron and hole quasi-equilibrium densities, i.e., $n_{11}^{e;\text{eq}}$ and $n_{11}^{h;\text{eq}}$, for a small average density of $n_0=0.001/a_B$ (dotted line) at a temperature of 50 K. Since the thermal energy $k_BT\approx 1E_B$ is smaller than the depth of the single-particle potential $\delta V(r_1,r_1)/2$ of $\approx 2E_B$, see Fig. 9(a), the quasi-equilibrium distributions are strongly concentrated in the regions of low potential energy, i.e., underneath the dielectric slabs. Due to the higher effective mass of the holes, the spatial variation of the hole distribution is steeper than that of the electron distribution in the regions underneath the dielectric–air interfaces (±45 nm in Fig. 9) where the single-particle potential changes rapidly.

The computed spatiotemporal dynamics of the electron density including dephasing and relaxation is displayed in Fig. 10. Compared to Fig. 5 we have used the same structural parameters and excitation conditions and only included the incoherent processes by using relaxation and nonradiative dephasing times of $T_1=T_2^*=6$ ps. These values are reasonable considering that excitonic transitions are excited with pulses of weak intensities. Figure 10 shows that immediately after the excitation the densities exhibit signatures of coherent wave packet dynamics, similar to Fig. 5. Due to relaxation and dephasing, this wave packet dynamics is damped with increasing time. In the limit of long times, i.e., $t \gg T_1, T_2^*$, the electron population approaches a quasi-equilibrium Fermi–Dirac distribution. Therefore, regardless of the excitation conditions which determine the position of the initially created density, the electrons eventually accumulate in the regions of low potential energy, i.e., underneath the dielectric slabs, cf. Fig. 9. This localization of the carrier densities makes such structures interesting for possible applications in laser structures. The fact that in the regions of high density, population inversion can be reached at a lower overall density can lead to a reduction of the laser threshold.[26,33]

IV. SUMMARY

It has been shown that surface polarizations at the interfaces between different dielectric materials may significantly modify the Coulomb interaction in their vicinity. As a result, both the band gap energy and the electron–hole attraction vary periodically in space near a photonic crystal. The modified Coulomb interaction leads to characteristic signatures in the excitonic absorption spectra of semiconductor photonic-crystal structures. In particular, the 1*s*-exciton resonance splits into a certain number of resonances with spatially inhomogeneous eigenfunctions.

Coherent excitation of the excitonic resonances leads to an intricate wave packet dynamics of the carrier distributions. This dynamics depends very sensitively on the central frequency of the laser pulses and also on their spectral width, since these parameters determine the strength with which a particular transition contributes to the coherent superposition. By using long laser pulses which are tuned to a specific excitonic resonance, carrier distributions which reflect the shape of a particular exciton wave function can be generated.

Due to dephasing and relaxation processes, the coherent wave packet dynamics is visible only in a certain time window after the optical excitation. With increasing time, the oscillations of the carrier densities are damped and in the limit of long times the carriers approach spatially inhomogeneous quasi-equilibrium distributions. This means that the carriers accumulate at the regions of low potential energy, i.e., underneath the dielectric slabs for the structures considered here. Further investigations of the optoelectronic properties of semiconductor photonic-crystal structures in the presence of spatially inhomogeneous carrier distributions are planned. In particular, investigations of possible superradiant light emission in structures with periodically varying space dependent densities would be very interesting.

ACKNOWLEDGMENTS

This work is supported by the Deutsche Forschungsgemeinschaft (DFG) through the Schwerpunktprogramm “Photonische Kristalle” and by the Center for Optodynamics, Philipps University, Marburg, Germany. T.M. thanks the DFG for support via a Heisenberg fellowship (ME 1916/1-1). We thank the John von Neumann Institut für Computing (NIC), Forschungszentrum Jülich, Germany, for grants for extended CPU time on their supercomputer systems.

---

[1] E. Yablonovitch, Phys. Rev. Lett. **58**, 2059 (1987).

[2] S. John, Phys. Rev. Lett. **58**, 2486 (1987).

[3] J. D. Joannopoulos, R. D. Meade, and J. N. Winn, *Photonic Crystals: Molding the Flow of Light* (Princeton University Press, Princeton, 1995).

[4] *Photonic Crystals and Light Localization in the 21st Century*, edited by C. Soukoulis (Kluwer Academic, Boston, 2001).

[5] *Photonic Crystals-Advances in Design, Fabrication and Characterization*, edited by K. Busch, S. Lölkes, R. B. Wehrspohn, and H. Föll (Wiley-VCH, Berlin, 2004).

[6] S. John and J. Wang, Phys. Rev. Lett. **64**, 2418 (1990).

[7] S. John and T. Quang, Phys. Rev. A **50**, 1764 (1994).

[8] T. Quang, M. Woldeyohannes, S. John, and G. S. Agarwal, Phys. Rev. Lett. **79**, 5238 (1997).

[9] P. R. Villeneuve, S. Fan, and J. D. Joannopoulos, Phys. Rev. B **54**, 7837 (1996).

[10] D. Labilloy, H. Benisty, C. Weisbuch, T. F. Krauss, R. M. De La Rue, V. Bardinal, R. Houdré, U. Oesterle, D. Cassagne, and C. Jouanin, Phys. Rev. Lett. **79**, 4147 (1997).

[11] O. Painter, R. K. Lee, A. Scherer, A. Yariv, J. D. O’Brien, P. D. Dapkus, and I. Kim, Science **284**, 1819 (1999).

[12] S. Noda, A. Chutinan, and M. Imada, Nature (London) **407**, 608 (2000).

[13] H. Haug and S. W. Koch, *Quantum Theory of the Optical and Electronic Properties of Semiconductors*, 4th ed. (World Scientific, Singapore, 2004).

[14] W. Schäfer and M. Wegener, *Semiconductor Optics and Transport Phenomena*, (Springer, Berlin, 2002).

[15] M. Imada, S. Noda, A. Chutinan, T. Tokuda, M. Murata, and G. Sadaki, Appl. Phys. Lett. **75**, 316 (1999).

[16] M. Boroditsky, T. F. Krauss, R. Coccioli, R. Vrijen, R. Bhat, and E. Yablonovitch, Appl. Phys. Lett. **75**, 1036 (1999).

[17] J.-K. Hwang, H.-Y. Ryu, D.-S. Song, I.-Y. Han, H.-W. Song, H.-G. Park, Y.-H. Lee, and D.-H. Jang, Appl. Phys. Lett. **76**, 2982 (2000).

[18] A. A. Erchak, D. J. Ripin, S. Fan, P. Rakich, J. D. Joannopoulos, E. P. Ippen, G. S. Petrich, and L. A. Kolodziejski, Appl. Phys. Lett. **78**, 563 (2001).

[19] H.-Y. Ryu, J.-K. Hwang, D.-S. Song, I.-Y. Han, and Y.-H. Lee, Appl. Phys. Lett. **78**, 1174 (2001).

[20] S. Noda, M. Yokoyama, M. Imada, A. Chutinan, and M. Mochizuki, Science **293**, 1132 (2001).

[21] D.-S. Song, S.-H. Kim, H.-G. Park, C.-K. Kim, and Y.-H. Lee, Appl. Phys. Lett. **80**, 3901 (2001).

[22] M. Kira, W. Hoyer, T. Stroucken, and S. W. Koch, Phys. Rev. Lett. **87**, 176401 (2001).

[23] T. Stroucken, R. Eichmann, L. Banyai, and S. W. Koch, J. Opt. Soc. Am. B **19**, 2292 (2002).

[24] R. Eichmann, B. Pasenow, T. Meier, T. Stroucken, P. Thomas, and S. W. Koch, Appl. Phys. Lett. **82**, 355 (2003).

[25] R. Eichmann, B. Pasenow, T. Meier, P. Thomas, and S. W. Koch, Phys. Status Solidi B **238**, 439 (2003).

[26] T. Meier and S. W. Koch, Ref. 5, Chap. 3, pp. 43–62.

[27] D. B. Tran Thoai, R. Zimmermann, M. Grundmann, and D. Bimberg, Phys. Rev. B **42**, 5906 (1990).

[28] L. V. Kulik, V. D. Kulakovskii, M. Bayer, A. Forchel, N. A. Gippius, and S. G. Tikhodeev, Phys. Rev. B **54**, R2335 (1996).

[29] R. H. Dicke, Phys. Rev. **93**, 99 (1954).

[30] T. Stroucken, A. Knorr, P. Thomas, and S. W. Koch, Phys. Rev. B **53**, 2026 (1996).

[31] A. Taflove, *Computational Electrodynamics-The Finite Difference Time-Domain Method* (Artech-House, Boston, 1995).

[32] W. H. Press, S. A. Teukolsky, W. T. Vetterling, and B. P. Flannery, *Numerical Recipes in C++* (Cambridge University Press,

Cambridge, 2002).

[33] M. Reichelt, B. Pasenow, T. Meier, T. Stroucken, and S. W. Koch, Phys. Rev. B **71**, 035346 (2005).

[34] E. O. Göbel, K. Leo, T. C. Damen, J. Shah, S. Schmitt-Rink, W. Schäfer, J. F. Müller, and K. Köhler, Phys. Rev. Lett. **64**, 1801 (1990).

[35] K. Leo, J. Shah, E. O. Göbel, T. C. Damen, S. Schmitt-Rink, W. Schäfer, and K. Köhler, Phys. Rev. Lett. **66**, 201 (1990).

[36] J. Feldmann, T. Meier, G. von Plessen, M. Koch, E. O. Göbel, P. Thomas, G. Bacher, C. Hartmann, H. Schweizer, W. Schäfer, and H. Nickel, Phys. Rev. Lett. **70**, 3027 (1993).

[37] W. Vogel and D. G. Welsch, *Quantum Optics* (Akademie, Berlin, 1994).

[38] A. Tip, Phys. Rev. A **56**, 5022 (1997).

[39] L. Banyai and S. W. Koch, *Semiconductor Quantum Dots* (World Scientific, Singapore, 1993).

[40] T. Meier and S. W. Koch, in *Ultrafast Physical Processes in Semiconductors*, special issue of Semiconductors and Semimetals Vol. 67 (Academic, New York, 2001), pp. 231–313.

[41] R. Loudon, Am. J. Phys. **44**, 1064 (1976).

[42] L. Banyai, I. Galbraith, C. Ell, and H. Haug, Phys. Rev. B **36**, 6099 (1987).

[43] S. W. Koch, T. Meier, F. Jahnke, and P. Thomas, Appl. Phys. A: Mater. Sci. Process. **71**, 511 (2000).

[44] I. Varga, P. Thomas, T. Meier, and S. W. Koch, Phys. Rev. B **68**, 113104 (2003).